International Journal of Machine Tools and Manufacture, Volume 51, Issue 6, June 2011, Pages 433-438

Author's Accepted Manuscript

www.elsevier.com/locate/ijmactool

Burn threshold prediction for high efficiency deep grinding

A. Bell, T. Jin, D.J. Stephenson

PII: S0890-6955(11)00019-8
DOI: doi:10.1016/j.ijmachtools.2011.01.006
Reference: MTM 2617

To appear in: *International Journal of Machine Tools & Manufacture*

Received date: 26 April 2010
Revised date: 12 January 2011
Accepted date: 13 January 2011

Cite this article as: A. Bell, T. Jin and D.J. Stephenson, Burn threshold prediction for high efficiency deep grinding, *International Journal of Machine Tools & Manufacture*, doi:10.1016/j.ijmachtools.2011.01.006

Burn Threshold Prediction for High Efficiency Deep Grinding

A.Bell, T. Jin and D. J. Stephenson

Cranfield University, Bedford, MK43 0AL

Abstract

Burn threshold diagrams are useful for the prediction of thermally induced grinding damage and were originally developed to describe the conventional shallow cut grinding regime. With the development of new high stock removal grinding processes such as high efficiency deep grinding (HEDG), the prevention of thermal damage to the workpiece is of particular concern. The principle of HEDG is based around the change in thermal characteristics of the grinding process at high Peclet numbers, whereby less heat is partitioned to the workpiece. Conventional burn threshold diagrams are valid for Peclet numbers below 50, well below the values expected in HEDG. This study presents a modified approach to the construction of burn threshold diagrams which takes account of the change in thermal partitioning with Peclet number. The approach has been validated through grinding trials over a range of specific material removal rates.

*Corresponding Author – now at The AMRC with Boeing, University of Sheffield, Wallis Way, Catcliffe,

S60 5TZ E: a.bell@amrc.co.uk T: +44(0)114 222 9590

Notation

a_e	Depth of cut
b_c	Width of cut
C	C-factor for grinding
c	Specific heat capacity of the workpiece material
d_e	Equivalent workpiece diameter
e_c	Specific grinding energy
$^{fi}/_{co}$	Ratio of the temperature in the contact surface to the temperature in the finished surface
k	Thermal conductivity
L	Peclet number
l_c	Wheel – workpiece contact length
P_w	Grinding power recorded
q_t^G	Dimensionless total heat flux generated during grinding
q_w^G	Dimensionless heat flux to the workpiece
R_w	Workpiece partition ration
α	Thermal diffusivity

β_w Thermal property = $\sqrt{k \cdot \rho \cdot c}$

$\bar{\theta}_m$ Maximum dimensionless temperature rise

θ_m Maximum temperature rise
θ_{ms} Maximum surface temperature rise
ρ Density of the workpiece material

Introduction

High Efficiency Deep Grinding (HEDG) is a novel abrasive machining process which readily achieves specific stock removal rates in excess of 50mm^3/mm·s whilst improving process efficiency and controlling surface integrity [1-5]. The high depths of cut, wheel and workpiece speeds fundamentally change the cutting and contact conditions and hence the thermal behaviour of the process. These fundamental changes to the thermal behaviour of the process can result in high temperatures in the wheel-workpiece contact zone, which facilitate the removal of surface material, but are subsequently removed with the grinding chip before significant penetration into the workpiece surface [6-8].

Residual stresses generated during grinding processes can have a detrimental effect on the performance and life of a ground component [9-11]. Significant reduction in fatigue life and the development of subsurface cracking are just a few of the problems likely to occur as a result of a poorly controlled grinding process. High temperatures resulting from the grinding process are also the primary driver for the generation of tensile residual stress [12-15].

A burn threshold diagram has been proposed in the literature [16,17] based on assumptions derived from conventional grinding processes and for Peclet numbers below 50 as shown in figure 1. Such diagrams are of particular use in defining the safe processing conditions to ensure that grinding temperatures do not exceed the burn threshold temperature for the workpiece. In constructing such diagrams it is assumed that all grinding energy except for 55% of the chip formation energy is transferred to the workpiece which is a reasonable assumption for typical shallow cut grinding conditions. However during HEDG processing as much as 95% of the total grinding energy can be removed with the grinding chip [6,8] and Peclet numbers readily exceed values of 50. It is therefore appropriate to reconsider the burn threshold diagram for HEDG processing conditions.

Development of a Burn Threshold Diagram for HEDG

The burn threshold diagram for the HEDG regime was initially developed following a similar process to that described by Malkin for shallow cut grinding [16,17]. Here, the maximum dimensionless temperature $\bar{\theta}_m$ is a function of the maximum temperature incurred, where:

$$\bar{\theta}_m = \frac{\pi \cdot k \cdot v_w}{2 \cdot \alpha \cdot \bar{q}_w} \cdot \theta_m \qquad (1)$$

α is the thermal diffusivity of the workpiece material and is defined by:

$$\alpha = \frac{k}{\rho \cdot c} \qquad (2)$$

Where k is the thermal conductivity, ρ is the density and c is the specific heat capacity of the workpiece material. The value v_w is the workpiece feedrate and q_w is the average heat flux entering the workpiece.

The maximum surface temperature θ_m for the HEDG regime is taken from the circular arc of heat contact model of Rowe & Jin [18] (figure 2) and is given by equation 3:

$$\theta_m = C \cdot \frac{\bar{q}_w}{\beta_w} \cdot \sqrt{\frac{l_c}{v_w}} \qquad (3)$$

Where l_c is the contact length between the wheel and workpiece, C is the temperature constant for workpiece thermal conduction quantifying the effect of contact angle and Peclet number on the contact zone temperature (figure 3) and β_w is described in equation 4:

$$\beta_w = \sqrt{k \cdot \rho \cdot c} \qquad (4)$$

Equation 1 can be rearranged in terms of the maximum surface temperature such that:

$$\theta_m = \bar{\theta}_m \cdot \frac{2 \cdot \alpha \cdot \bar{q}_w}{\pi \cdot k \cdot v_w} \qquad (5)$$

Combining equations 3 and 5 produces the following relationship:

$$\theta_m = \bar{\theta}_m \cdot \frac{2 \cdot \alpha \cdot \bar{q}_w}{\pi \cdot k \cdot v_w} = C \cdot \frac{\bar{q}_w}{\beta_w} \cdot \sqrt{\frac{l_c}{v_w}} \qquad (6)$$

Equation 6 can be rearranged to give the dimensionless temperature in terms of the grinding variables and thermal properties of the workpiece, where:

$$\bar{\theta}_m = C \cdot \frac{\bar{q}_w}{\beta_w} \cdot \frac{\pi \cdot k \cdot v_w}{2 \cdot \alpha \cdot \bar{q}_w} \cdot \sqrt{\frac{l_c}{v_w}} \qquad (7)$$

Given that the Peclet number L is defined as:

$$L = \frac{v_w \cdot l_c}{4 \cdot \alpha} \qquad (8)$$

Equation 7 can be reduced to give the dimensionless temperature in simple terms:

$$\bar{\theta}_m = C \cdot \pi \cdot L^{1/2} \qquad (9)$$

Malkin & Lenz [16] demonstrated a graphical relationship between the Peclet number and the dimensionless surface temperature. This is a derivation of the Jaeger model [19] and forms the basis of the development of the burn threshold diagram. Figure 4 shows the original relationship presented by Malkin [17] compared to that derived from the circular arc of heat contact model. It can be seen that the new relationship deviates from the original as a result of the inclusion of the C-factor and that this deviation becomes more significant as the Peclet number is increased into the HEDG regime at values typically in excess of 40.

Following the methodology suggested by Malkin [17], equations 1 and 9 are combined, such that:

$$\bar{\theta}_m = \frac{\pi \cdot k \cdot v_w}{2 \cdot \alpha \cdot \bar{q}_w} \cdot \theta_m = C \cdot \pi \cdot L^{1/2} \qquad (10)$$

This can be rearranged to give the maximum contact temperature in terms of Peclet number L, where:

$$\theta_m = \frac{2 \cdot \alpha \cdot \bar{q}_w}{k \cdot v_w} \cdot C \cdot L^{1/2} \qquad (11)$$

Expanding the Peclet number gives the temperature in terms of basic grinding parameters:

$$\theta_m = \frac{2 \cdot \alpha \cdot \bar{q}_w}{k \cdot v_w} \cdot C \cdot \left(\frac{v_w \cdot l_c}{4 \cdot \alpha} \right)^{1/2} \qquad (12)$$

Contact length is estimated by:

$$l_c = \left(a_e \cdot d_e \right)^{1/2} \qquad (13)$$

Where a_e is the depth of cut and d_e is the equivalent wheel diameter, for surface grinding this is equal to the wheel diameter.

Substitution into (12) gives:

$$\theta_m = \frac{2 \cdot \alpha \cdot \bar{q}_w}{k \cdot v_w} \cdot C \cdot \left(\frac{v_w \cdot a_e^{1/2} \cdot d_e^{1/2}}{4 \cdot \alpha} \right)^{1/2} \qquad (14)$$

Simplifying equation 14, θ_m can be rewritten as:

$$\theta_m = \frac{C \cdot \alpha^{1/2} \cdot \overline{q}_w \cdot a_e^{1/4} \cdot d_e^{1/4}}{k \cdot v_w^{1/2}} \qquad (15)$$

The mean heat flux in the contact zone in the circular arc of heat contact model is described in terms of the total heat flux, where:

$$\overline{q}_w = R_w \cdot \overline{q}_t \qquad (16)$$

R_w is an estimation of the energy partition coefficient to the workpiece and is a factor dependent upon the contact conditions and material. In this review, values of R_w are determined using the methodology presented by Stephenson & Jin [20].

Substituting equation 16 into equation 15 gives:

$$\theta_m = \frac{C \cdot \alpha^{1/2} \cdot R_w \cdot \overline{q}_t \cdot a_e^{1/4} \cdot d_e^{1/4}}{k \cdot v_w^{1/2}} \qquad (17)$$

The total heat flux $\overline{q}_t$ can be written in terms of the grinding parameters, where:

$$\overline{q}_t = e_c \cdot a_e \cdot \frac{v_w}{l_c} \qquad (18)$$

The specific grinding energy e_c is calculated from the grinding variables and the monitored grinding power P_w using equation 19:

$$e_c = \frac{P_w}{v_w \; a_e \; b_c} \qquad (19)$$

Where b_c is the grinding width.

Recalling equation 13 and substituting equation 18 into equation 17 gives:

$$\theta_m = \frac{C \cdot \alpha^{1/2} \cdot R_w \cdot v_w^{1/2} \cdot a_e^{3/4} \cdot e_c}{k \cdot d_e^{1/4}} \qquad (20)$$

Grinding burn occurs on the finished workpiece surface depending on the temperature. The above derivation yields equations that predict the maximum contact temperature, which is appropriate if one assumes all the thermal energy in the contact surface is transferred to the finished workpiece surface. The circular arc of heat contact model considers the relationship between contact and finished surface temperatures through the factor $^{fi}/_{co}$, which accounts for the angle of inclination of the contact surface and the effect of workpiece speed through the Peclet number. Therefore the maximum surface temperature can be described as:

$$\theta_{ms} = \frac{{}^{fi}/_{co} \cdot C \cdot \alpha^{1/2} \cdot R_w \cdot v_w^{1/2} \cdot a_e^{3/4} \cdot e_c}{k \cdot d_e^{1/4}} \qquad (21)$$

Equation 21 can be rearranged to give temperature change in terms of specific grinding energy, where:

$$e_c = \frac{\theta_{ms} \cdot k}{A \cdot \alpha^{1/2}} \cdot d_e^{1/4} \cdot v_w^{-1/2} \cdot a_e^{-3/4} \qquad (22)$$

Where A is a dimensionless variable relating to contact and material condition and is equal to:

$$A = {}^{fi}/_{co} \cdot C \cdot R_w \qquad (23)$$

Values of C and ${}^{fi}/_{co}$ were calculated as a function of contact angle and Peclet number using the circular arc of heat contact model [18].

Figure 5 applies the new approach to the grinding of SG cast iron using the conditions summarised in Table 1 and demonstrates the variation between the two predicted burn threshold lines for a limiting temperature rise of 150°C. The resultant boundary lines represent the minimum specific grinding energy required for the grinding parameters to give rise to a damaged workpiece surface. During the transition from conventional to HEDG grinding regimes, the model correctly predicts the occurrence of burn at very low values of specific grinding energy, before the HEDG effect becomes prevalent. A fundamental change in the threshold condition is experienced at the high removal rates represented by very low values on the abscissa. This behaviour is the result of the change in energy partitioning and increases in contact angle and Peclet number associated with the HEDG regime. As specific material removal rates increase into HEDG conditions the temperature in the finished surface is reduced by an increase in the heat flux to the chip and the favourable contact angle.

Material	a_e (mm)	b (mm)	v_w (mm/min)	v_s (m/s)	Q'_w (mm^3/mm·s)
SGCI	0.5 – 7	5	2500	150	20 – 300

Table 1 Grinding parameters for plot of $d_e^{1/4} \cdot a_e^{-3/4} \cdot v_w^{-1/2}$ versus Specific Grinding Energy

Experimental Validation

Experimental validation was undertaken on an Edgetek Superabrasive surface grinding machine designed for the application of the HEDG process. Samples of SG Cast Iron were mounted in a workpiece fixture and ground in the down grinding mode. Grinding parameters are detailed in Table 2.

a_e (mm)	b (mm)	v_w (mm/min)	v_s (m/s)
0.5 – 9	5 – 2	50 – 7500	50 – 150

Table 2 Summary of grinding parameters for burn threshold diagram trials

Application of the new burn threshold methodology to results for the grinding of SG Cast Iron suggested a burn threshold temperature rise of 150°C. Grinding burn was determined to have occurred with the onset of temper discoloration in the ground surface, which can occur at lower temperatures than would cause potential damage; typical temper discoloration for SG Cast Iron is shown in figure 6. Using equation 22, lines of constant temperature were estimated and a constant temperature threshold line of 150°C was determined. This threshold line provided the best fit between the burnt and unburnt samples. Figures 7 to 9 describe the burn threshold curve for values of grinding parameters at wheel speeds of 50ms/, 100m/s and 150 m/s as the curve geometry is variable with wheel speed. This demonstrates the boundary separating the regions of burnt and unburnt surfaces offers a reliable predictive capability under HEDG conditions by taking into account the change in energy partitioning and increases in contact angle and Peclet number.

Given knowledge of the grinding parameters and the estimated value of specific grinding energy from relationships presented by Stephenson & Jin [20], the occurrence of grinding burn may be predicted. Improving accuracy of the burn threshold line by incorporating the latest in thermal modelling techniques allows for a better definition of the burnt and unburnt regions. This becomes increasingly relevant when considering that under aggressive grinding conditions relatively small changes in specific grinding energy can result in large changes in surface temperature moving components rapidly into burnt regions. Therefore a reliable and easy method of predicting the boundary is imperative for the creation of a robust method and ultimately successful industrial application of the burn threshold technique.

Conclusions

By considering the fundamental changes in thermal behaviour which result from the HEDG process it has been possible to develop a new relationship between the process variables and the specific grinding energy. This relationship produces an inflected curve, which allows for an increased specific grinding energy before the occurrence of grinding burn when in the HEDG regime.

Experimental results for SG Cast Iron demonstrate a good correlation with a predicted boundary for a 150°C temperature rise. This temperature rise was estimated from the best fit between burnt and unburnt samples when workpieces were inspected visually. The temperature rise may be considered low; however, it is of an appropriate magnitude for the material in question.

Further work is required to validate this approach fully with a test programme utilising a quantitative method of burn validation such as x-ray diffraction or magnetic Barkhausen noise analysis. This work will determine if threshold temperatures are related to time temperature transformation data for specific materials.

References

1) T. Tawakoli, High Efficiency Deep Grinding, VDI-Verlag, Dusseldorf, 1993.
2) T. Jin, D.J. Stephenson, J. Corbett, Burn threshold of high carbon steel in High Efficiency Deep Grinding, P. I. Mech. Eng. B-J. Eng. 216 (2002) 357-364.
3) D.J. Stephenson, T. Jin, J. Corbett, High Efficiency Deep Grinding of a Low Alloy Steel with Plated CBN Wheels, CIRP Annals. 51/1 (2002) 241-244.
4) D.J. Stephenson, P. Comley, High Performance Superabrasive Grinding, Proceedings of the 4th International Conference on Leading Edge Manufacturing in 21st Century, Fukuoka, Japan, 7-9 November 2007.
5) I. Walton, D.J. Stephenson, A. Baldwin, The measurement of grinding temperatures at high specific material removal rates, Int. J. Mach. Tool. Manu. 46 (2005) 1617-1625.
6) T. Jin, D.J. Stephenson, Investigation of the Heat Partitioning in High Efficiency Deep Grinding, Int. J. Mach. Tool. Manu. 43 (2003) 1129-1134.
7) T. Jin, D.J. Stephenson, Three Dimensional Finite Element Simulation of Transient Heat Transfer in High Efficiency Deep Grinding, CIRP Annals. 53/1 (2004) 259-262.
8) T. Jin, D.J. Stephenson, Analysis of grinding chip temperature and energy partitioning in High Efficiency Deep Grinding, P. I. Mech. Eng. B-J. Eng. 220/5 (2006) 615-625.
9) N. Eliaz, H. Sheinkopf, G. Shemesh, H. Artzi, Cracking in cargo aircraft main landing gear truck beams due to abusive grinding following chromium plating, Eng. Fail. Anal. 12 (2005) 337-347.
10) F.S. Silva, Analysis of a vehicle crankshaft failure, Eng. Fail. Anal. 10 (2003) 605-616
11) E. Brinksmeier, T.J. Cammett, W. Konig, P. Leskovar, J. Peters, H.K. Tonshoff, Residual Stresses - Measurement and Causes in Machining Processes, CIRP Annals. 31/2 (1982) 491-510.
12) X. Chen, W.B. Rowe, D.F. McCormack, Analysis of the transitional temperature for tensile residual stress in grinding, J. Mater. Process. Tech. 107 (2000) 216-221.
13) M. Mahdi, L.C. Zhang, Residual Stresses in Ground Components caused by Coupled Thermal and Mechanical Plastic Deformation, J. Mater. Process. Tech. 95 (1999) 238-245.
14) M. Mahdi, L. Zhang, Applied mechanics in grinding. Part 7: residual stresses induced by the full coupling of mechanical deformation, thermal deformation and phase transformation, Int. J. Mach. Tool. Manu. 39 (1999) 1285-1298.
15) R. Snoeys, M. Maris, J. Peters, Thermally induced damage in grinding, CIRP Annals. 27/2 (1978) 571-581.
16) S. Malkin, E. Lenz, Burning Limit for Surface and Cylindrical Grinding of Steels, CIRP Annals, 27/1 (1978) 233-236.
17) S. Malkin, Grinding Technology: theory and applications of machining with abrasives, Society of Manufacturing Engineers, Michigan, 1989.
18) W.B. Rowe, T. Jin, Temperatures in High Efficiency Deep Grinding (HEDG), CIRP Annals, 27/1 (2001) 205-208.
19) J.C. Jaeger, Moving Sources of Heat and the Temperature at Sliding Contacts, Proceedings of the Royal Society of New South Wales, 76 (1942) 203-224.
20) D.J. Stephenson, T. Jin, Physical Basics in Grinding, European Conference on Grinding, WZL Aachen, 6-7 November 2003.

Captions

Figure 1: Burn threshold diagram after Malkin [17]

Figure 2: Circular arc of heat contact model after Rowe & Jin [18]

Figure 3: Graphical representation of the C-factor after Rowe & Jin [18]

Figure 4: Comparison of the relationship between Peclet number and dimensionless temperature for the new relationship presented in equation 9 versus the original relationship presented by Malkin & Lenz [16]

Figure 5: Limiting threshold curves for a temperature rise of 150ºC, comparing the original Malkin model to the model described in equation 22 and demonstrating grinding burn at very low values of specific grinding energy, which occur during the transition from conventional to HEDG grinding regimes

Figure 6: Sample burnt surfaces in SG Cast Iron showing typical temper discoloration

Figure 7: Burn threshold diagram demonstrating a limiting threshold for a temperature rise of 150ºC for wheel speeds of 50m/s

Figure 8: Burn threshold diagram demonstrating a limiting threshold for a temperature rise of 150ºC for wheel speeds of 100m/s

Figure 9: Burn threshold diagram demonstrating a limiting threshold for a temperature rise of 150ºC for wheel speeds of 150m/s

Figure 1

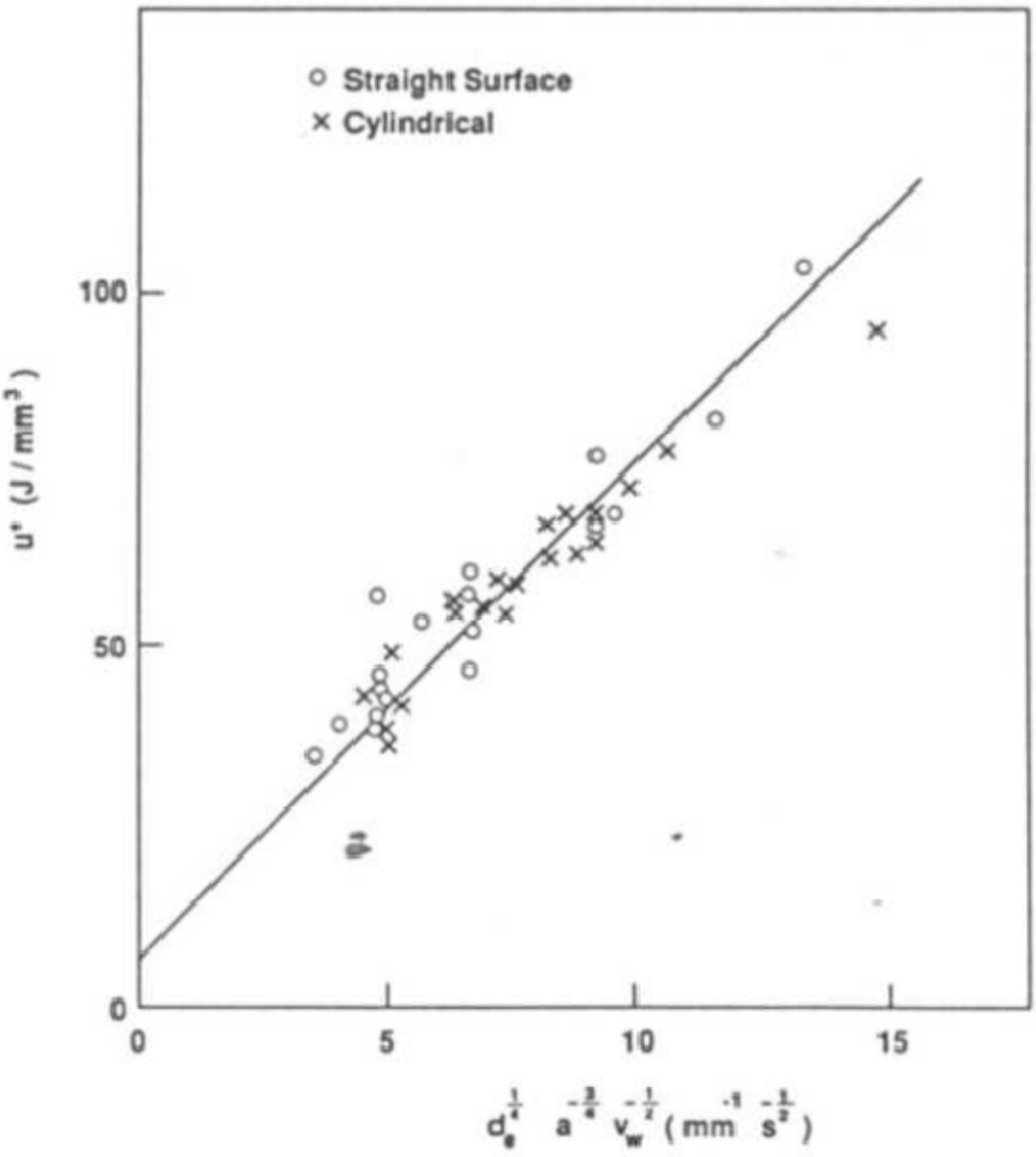

Figure 2

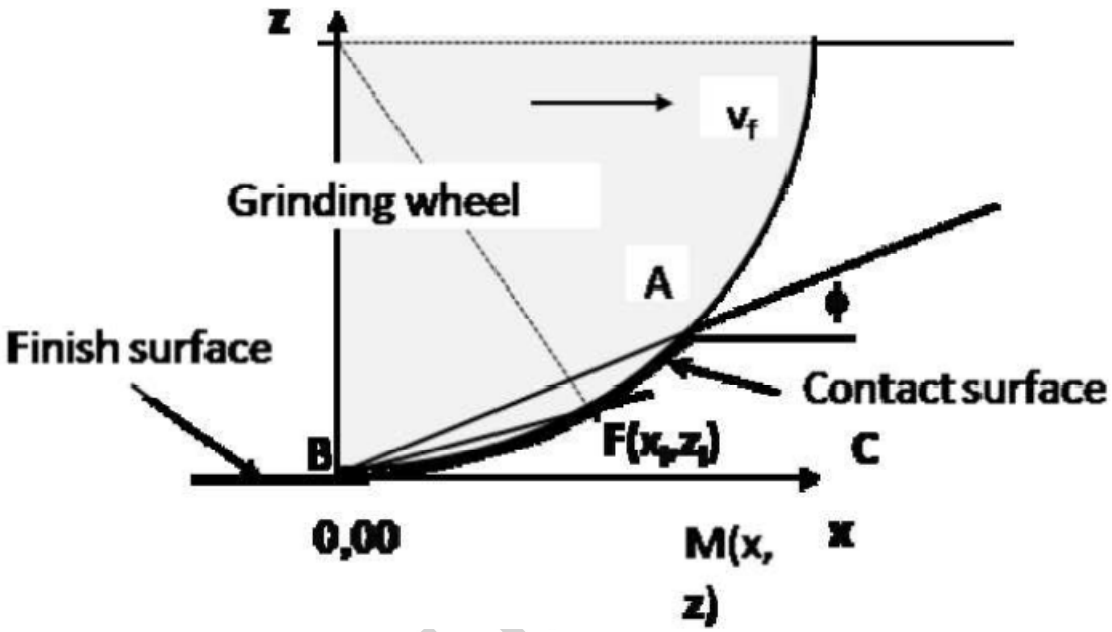

Figure 3

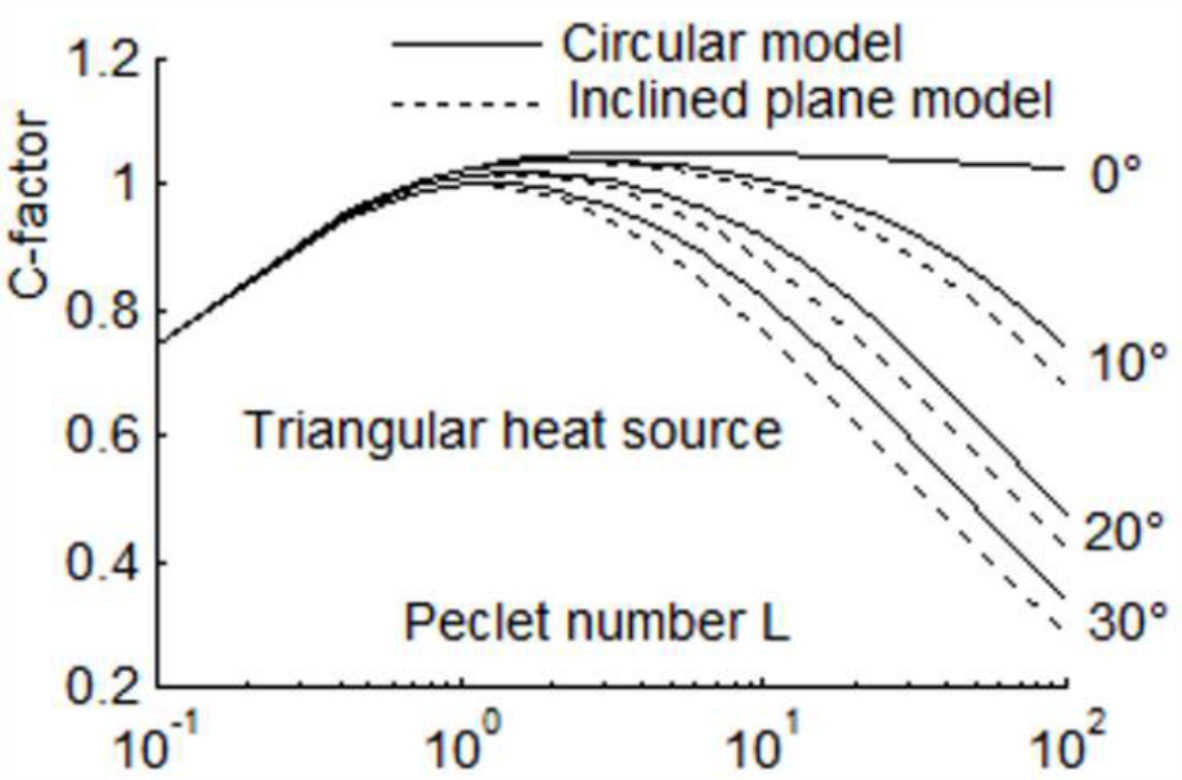

Figure 4

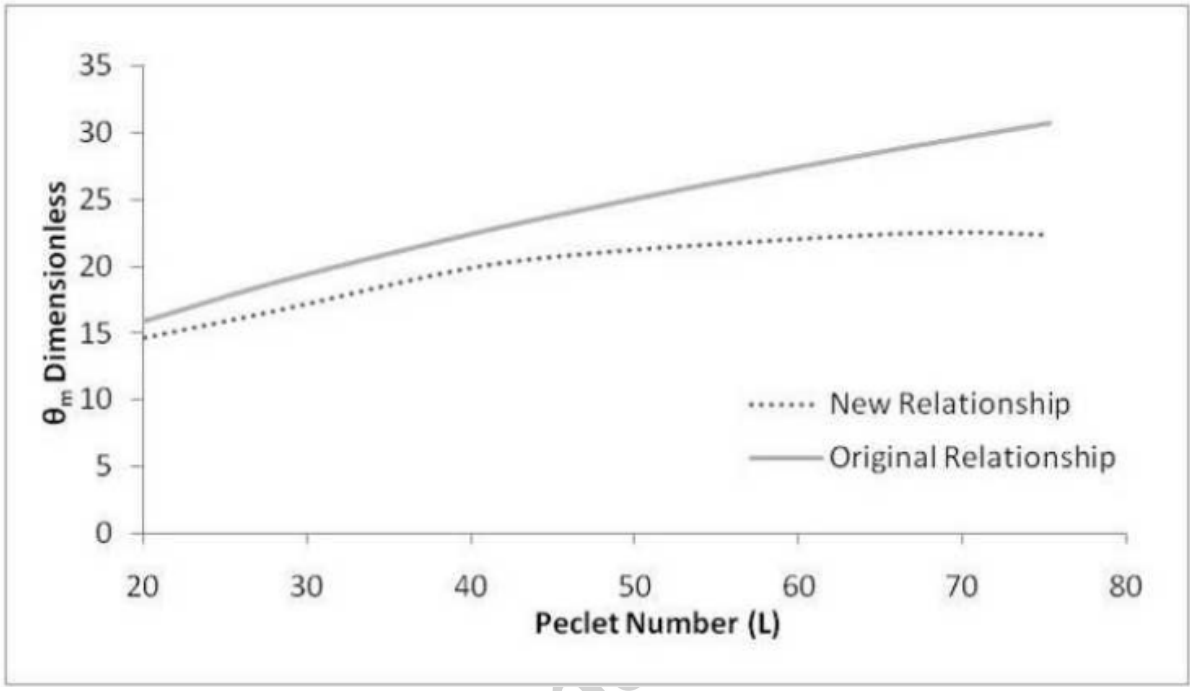

Figure 5

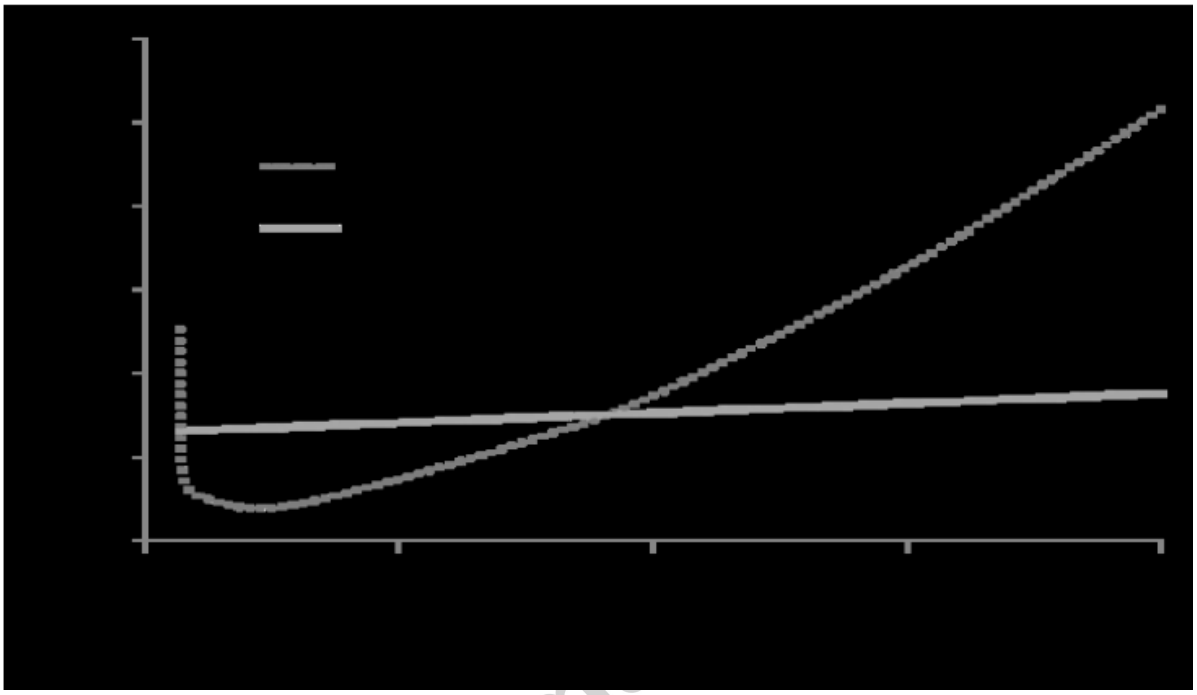

Figure 6

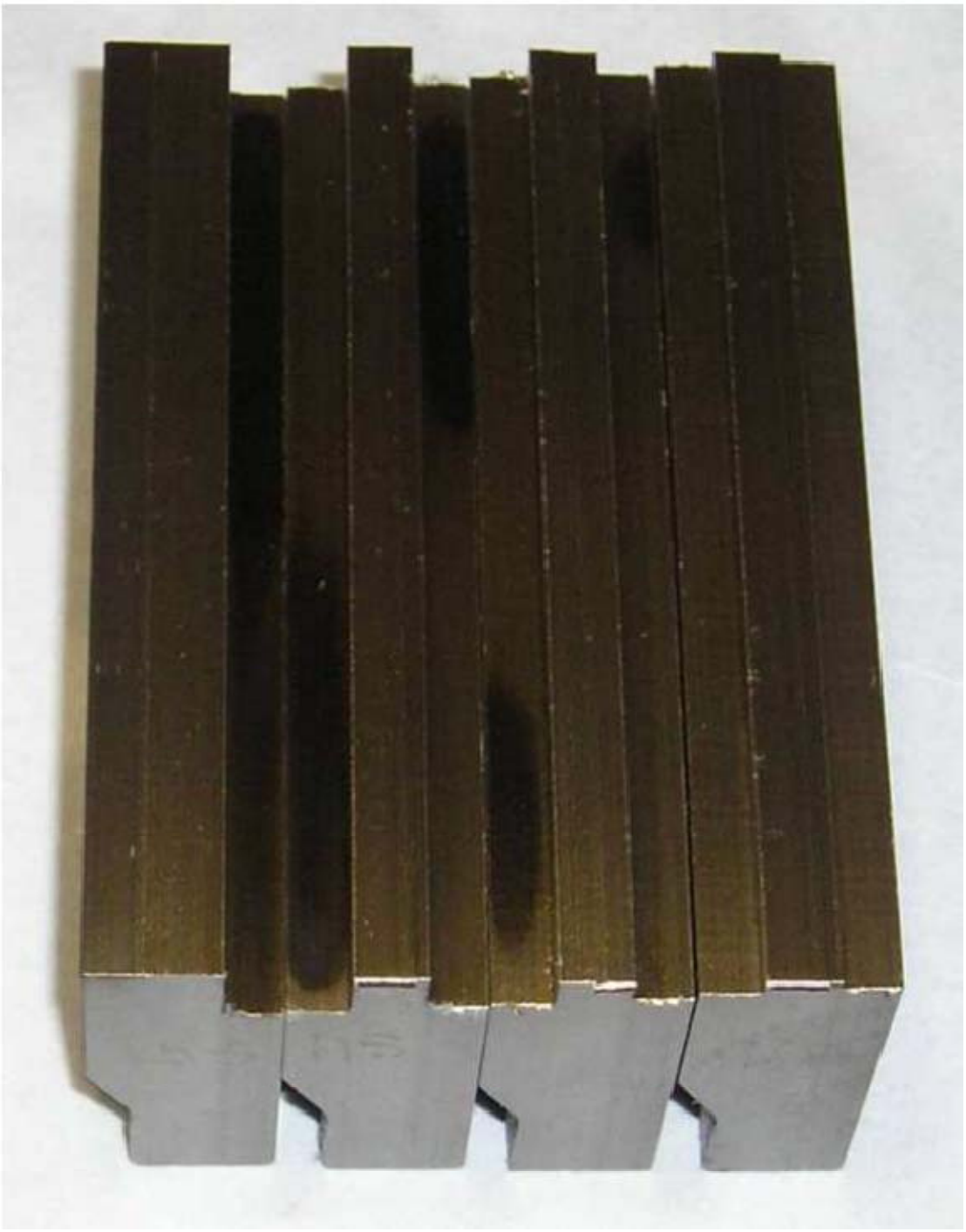

Figure 7

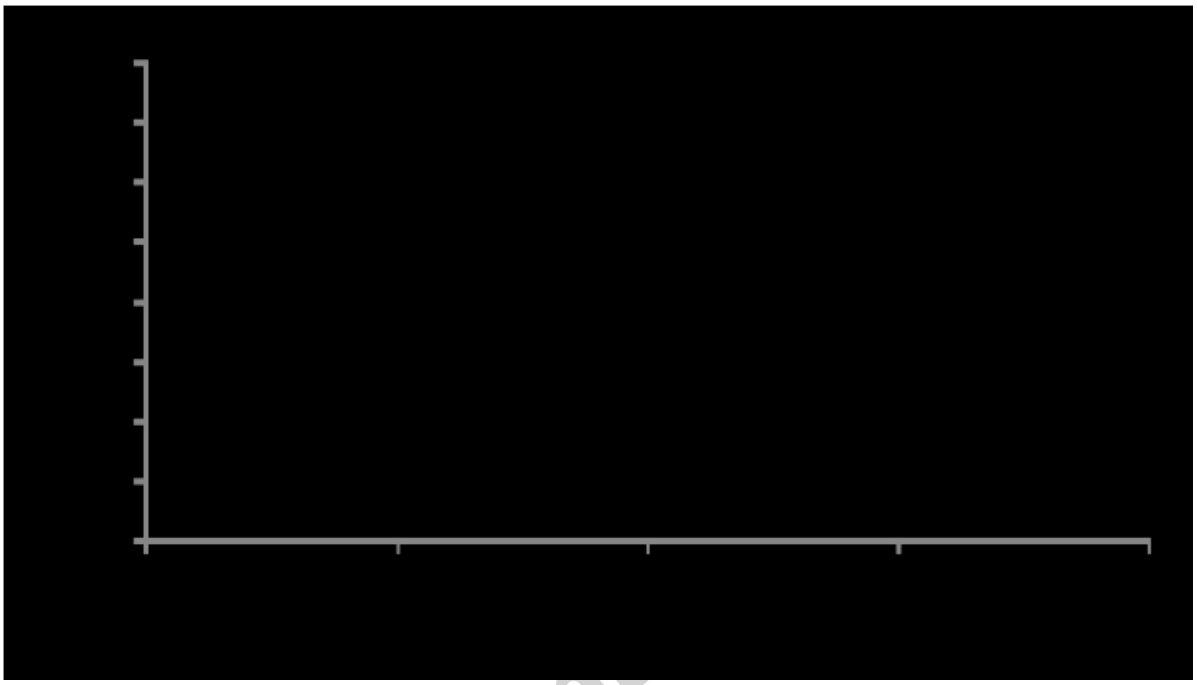

Figure 8

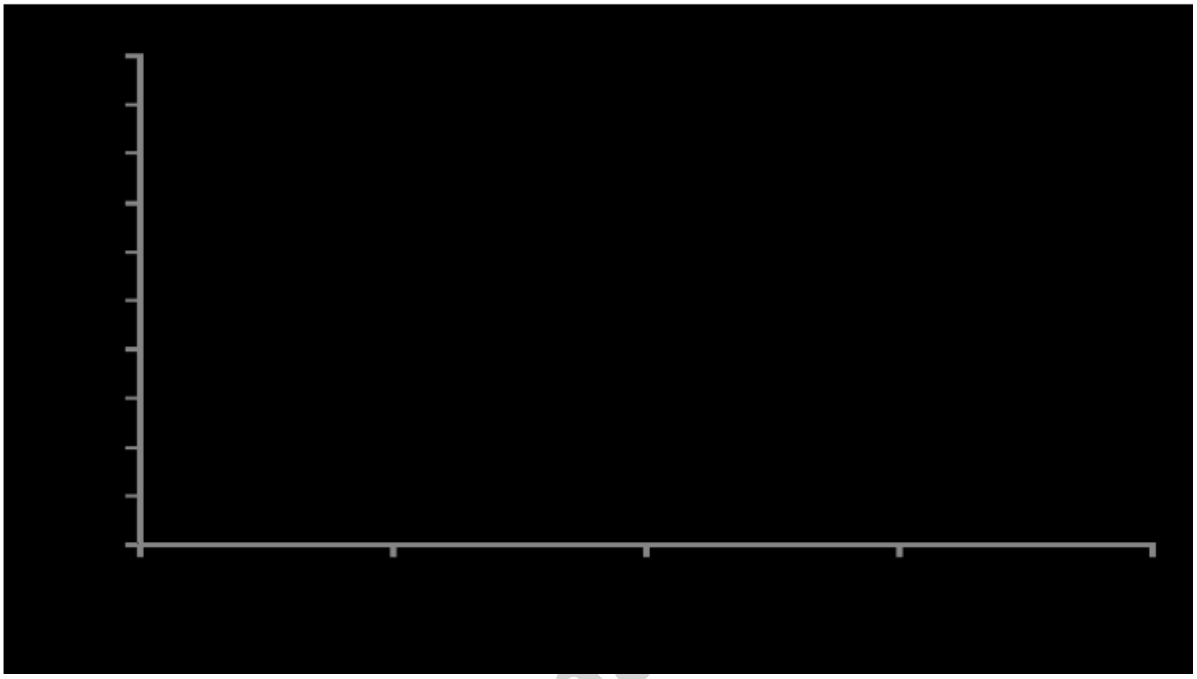

Figure 9